nature climate change

ARTICLES

https://doi.org/10.1038/s41558-020-0822-0

Warming trends increasingly dominate global ocean

Gregory C. Johnson[1]✉ and John M. Lyman[1,2]

The ocean takes up about 93% of the global warming heat entering Earth's climate system. In addition, the associated thermal expansion contributes substantially to sea-level rise. Hence, quantifying the oceanic heat uptake rate and its statistical significance has been a research focus. Here we use gridded ocean heat content maps to examine regional trends in ocean warming for 0–700 m depth from 1993–2019 and 1968–2019, periods based on sampling distributions. The maps are from four research groups, three based on ocean temperature alone and one combining ocean temperature with satellite altimeter sea-level anomalies. We show that use of longer periods results in larger percentages of ocean area with statistically significant warming trends and less ocean area covered by statistically significant cooling trends. We discuss relations of these patterns to climate phenomena, including the Pacific Decadal Oscillation, the Atlantic Meridional Overturning Circulation and global warming.

An ongoing increase of GHG concentrations in the atmosphere coupled with the long response timescales and large thermal capacity of the oceans and the cryosphere have led to an energy imbalance: less energy leaves Earth's climate system than enters it. From 1971 to 2010, around 93% of this excess energy went into warming the oceans, with 3% melting ice, 3% warming the land and only 1% warming and moistening the atmosphere (where the latent heat energy for evaporation to maintain relative humidity is roughly equivalent to the energy to warm the atmosphere)[1]. Furthermore, ocean warming is tightly linked to sea-level rise, with expansion owing to that warming accounting for about 42% of global average sea-level rise since 1993 (ref. [2]). Thus, global depth-integrated ocean temperature change is a key metric of a changing climate[3], with ocean warming tightly linked to increases in atmospheric GHG concentrations.

The IPCC Fifth Assessment Report estimated the global energy imbalance for 2005–2010, which as noted is dominated by ocean warming, as equivalent to 0.6 (±0.4) watts per square metre (W m^{-2}) applied over the entire surface area of Earth (their fig. 2.11)[1]. Argo measurements since 2010 have greatly narrowed the uncertainty of estimates of ocean heat uptake, so that the global energy imbalance for 2005–2016 has been estimated as 0.7 (±0.1) W m^{-2} in one study[4]. The ocean heat uptake values in that study over the Argo sampling range for similar periods are in good agreement with those reported in other studies[5,6].

Determining rates of globally integrated ocean heat content is not a trivial task as ocean temperature measurements have been made with a wide variety of instruments, with varying accuracy, to varying depths and at varying spatial and temporal resolution[7]. Historical data coverage generally wanes back in time, towards the south and with increasing depth[3,7,8]. With the advent of the expendable bathythermograph (XBT), the upper 450 m of the ocean began to be sampled widely around 1968, at least in the shipping lanes to around 30° S. By about 1993, deep XBTs measuring to 700 m depth were in common use, largely owing to the efforts of the World Ocean Circulation Experiment. The Argo array of profiling floats first reached sparse global coverage in 2005 or 2006, accurately measuring ocean temperatures to nearly 2,000 m (ref. [9]).

Regional subsurface ocean temperature (as well as subsurface salinity and sea level) distributions also vary substantially with climate phenomena or patterns such as El Niño[10,11], the Pacific Decadal Oscillation (PDO)[12,13], the North Atlantic Oscillation[14] and other large-scale variations in wind stress over the ocean, for example, in the South Pacific[15]. These prominent variations of subsurface ocean temperature associated with large-scale changes in winds and currents, as well as air–sea heat fluxes, over timescales from interannual to multidecadal, mean that regional ocean temperature (and sea level) trends are often larger and less certain than global integrals of those quantities[16]. Studies of sea level in climate simulations suggest that it can take from decades to nearly a century to detect the long-term GHG forced signal of sea level locally in the face of these other presumably natural variations, with the detection time dependent on the region[17].

Here we pose intermediate questions regarding ocean warming. What fraction of the upper ocean (used here to mean 0–700 m depth) exhibits a statistically significant warming or cooling trend (without formal attribution) over periods varying from 5 yr (arguably the shortest period over which one could compute statistical significance of a trend) to the record length? How do the large-scale patterns of variability in upper-ocean heat content trends over the record length relate to prominent climate phenomena, both natural and anthropogenic?

To investigate those questions we generate maps of annual upper-ocean heat content anomalies from 1993 to 2019 by combining sea level anomaly data from satellite altimeters with ocean temperature data[18,19], hereafter denoted PMEL maps (for the National Oceanic and Atmospheric Administration's (NOAA's) Pacific Marine Environmental Laboratory) and use upper-ocean annual maps from ocean temperature data from three other research groups, hereafter denoted JMA[20] (for Japan Meteorological Agency), IAP[21] (for Institute of Atmospheric Physics, Chinese Academy of Sciences) and NCEI[22] (for NOAA's National Center for Environmental Information) for analyses spanning the years 1993–2019 and 1968–2019. The selection of these periods is motivated by improvements in the observational record in 1968 and again in 1993 (ref. [8]). The 1993–2019 maps are more robust, but analysing

[1]NOAA/Pacific Marine Environmental Laboratory, Seattle, WA, USA. [2]Joint Institute for Marine and Atmospheric Research, University of Hawai'i at Manoa, Honolulu, HI, USA. ✉e-mail: gregory.c.johnson@noaa.gov

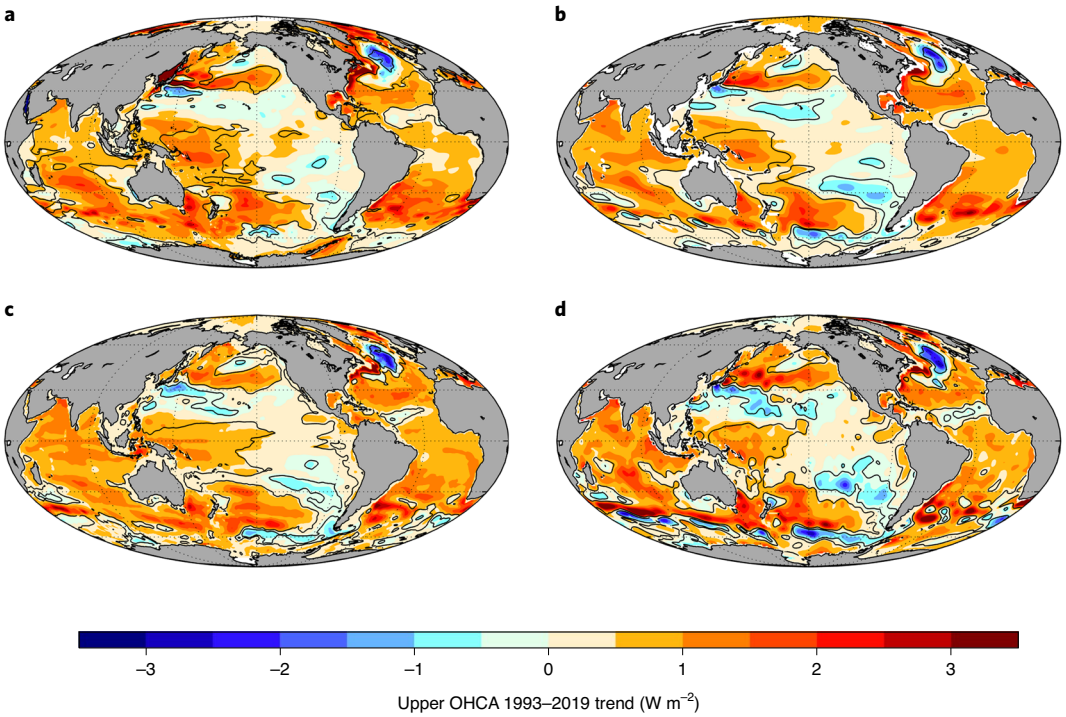

Fig. 1 | Upper-ocean heat content anomaly linear trends for 1993–2019. a–d, For annual estimates of the PMEL combined maps (**a**) and the in situ-only maps of JMA (**b**), IAP (**c**) and NCEI (**d**). Values are in W m^{-2} (colour bar) applying 90% two-tailed (5–95%) confidence limits to outline areas with trends that are statistically significantly different from zero (black contours). Latitudes are gridded at 30° intervals, and longitudes, centered on 150 °W, at 60° intervals (dotted lines). OHCA, ocean heat content anomaly.

1968–2019 provides some useful insights. We then analyse trends from the record lengths (27 and 52 yr) down to 5-yr intervals, assessing their regional statistical significance.

Ocean warming trends for 1993–2019 PMEL maps are skewed, with 16% of the area occupied by negative trends and 84% by positive trends (Fig. 1a). However, these trends are not everywhere statistically significantly different from zero (see Methods). Limiting the area to statistically significant regions results in 56% of the ocean surface analysed being covered by significant positive trends, but only 3% of the ocean surface area by significant negative trends (Fig. 1a, black contours; Table 1), even more skewed towards positive values than the analysis without regard to statistical significance. Local values of the 27-yr trends range from a minimum of −8 W m^{-2} to a maximum of 7 W m^{-2} for the PMEL maps, much larger than the average trend for the ocean surface area of 0.60 W m^{-2} (equivalent to 0.42 W m^{-2} applied uniformly over Earth's surface). By comparison, trends for 90% of the ocean area analysed lie between −0.4 and 1.8 W m^{-2}, again skewed towards positive values.

Areas of statistically significant ocean-warming trends for 1993–2019 are similarly skewed for the other maps (Fig. 1b–d and Table 1), with the largest skewness for IAP maps (68% positive and 5% negative) and the smallest for NCEI maps (57% positive and 10% negative). For the longer period of 1968–2019 (Fig. 2 and Table 1), the areas with statistically significant positive trends become even larger, and those with statistically significant negative trends even smaller. Again, for 1968–2019 trends, IAP maps are the most skewed (80% positive and 1% negative) and NCEI maps the least skewed (72% positive and 3% negative). There are not PMEL maps for this period, since satellite altimetry began around 1993, and the PMEL maps incorporate satellite altimetry data.

Calculating the statistically significant areas with positive and negative trends for each of the possible 5-yr trend estimates, 6-yr trend estimates and so on to the one possible 27-yr (or 52-yr) trend estimate reveals that the longer the period used for the trend estimates, the larger the ocean surface area occupied by statistically significant warming, whatever group's maps are used (Fig. 3). We deem 5 yr the shortest period for which statistical significance of a trend might plausibly be estimated. For 1993–2019 (Fig. 3a), the average of the 5-yr trend maps (they provide only about 5.4 degrees of freedom because of substantial overlaps in time of successive 5-yr periods) with statistically significant warming and cooling areas amounts to 24% and 17%, respectively, for the PMEL (combined) map, with similar values for the other (in situ-only) maps. The increases in areas with statistically significant warming trends and decreases in areas with statistically significant cooling trends with

Table 1 | Fractional areas of statistically significant positive and negative trends for upper-ocean heat content anomalies

Product	Period	Significantly positive trend	Significantly negative trend
PMEL	1993–2019	56%	3%
JMA	1993–2019	58%	8%
IAP	1993–2019	68%	5%
NCEI	1993–2019	57%	10%
JMA	1968–2018	79%	1%
IAP	1968–2018	80%	1%
NCEI	1968–2019	72%	3%

Annual maps from four research groups are used, with two record lengths (1993–2019 and 1968–2019) shown.

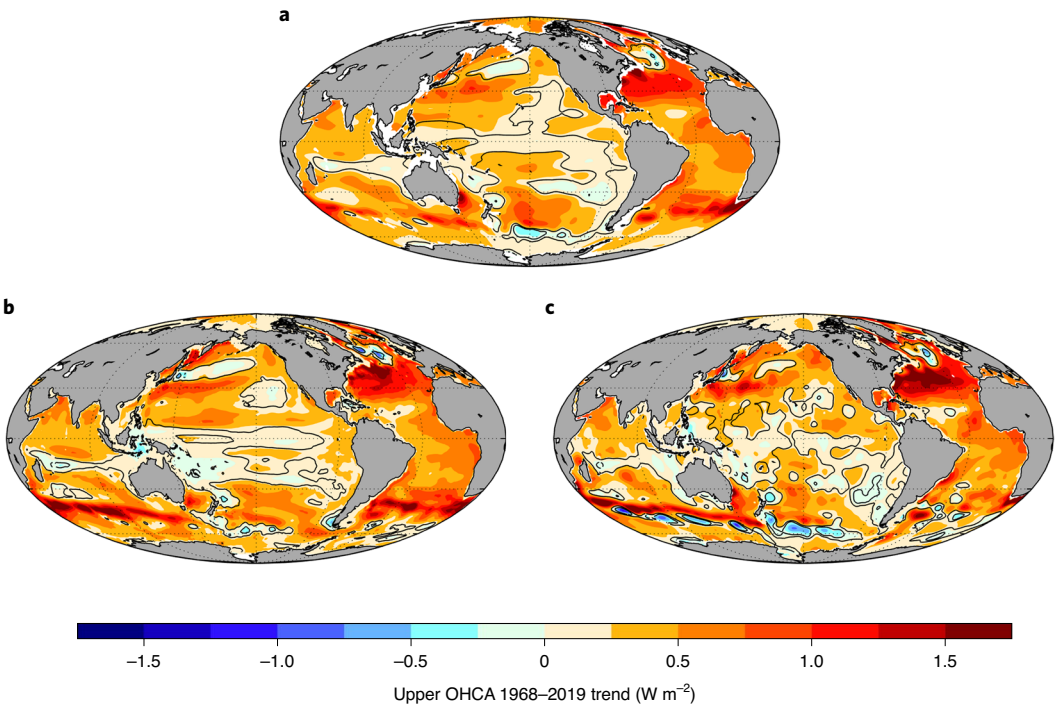

Fig. 2 | Upper-ocean heat content anomaly linear trends for 1968–2019. a–c, For annual estimates using the in situ-only maps of JMA (**a**), IAP (**b**) and NCEI (**c**). Values are in W m^{-2} (colour bar) applying 90% two-tailed (5–95%) confidence limits to outline areas with trends that are statistically significantly different from zero (black contours). Latitudes are gridded at 30° intervals, and longitudes, centered on 150 °W, at 60° intervals (dotted lines). The scale is half that of Fig. 1.

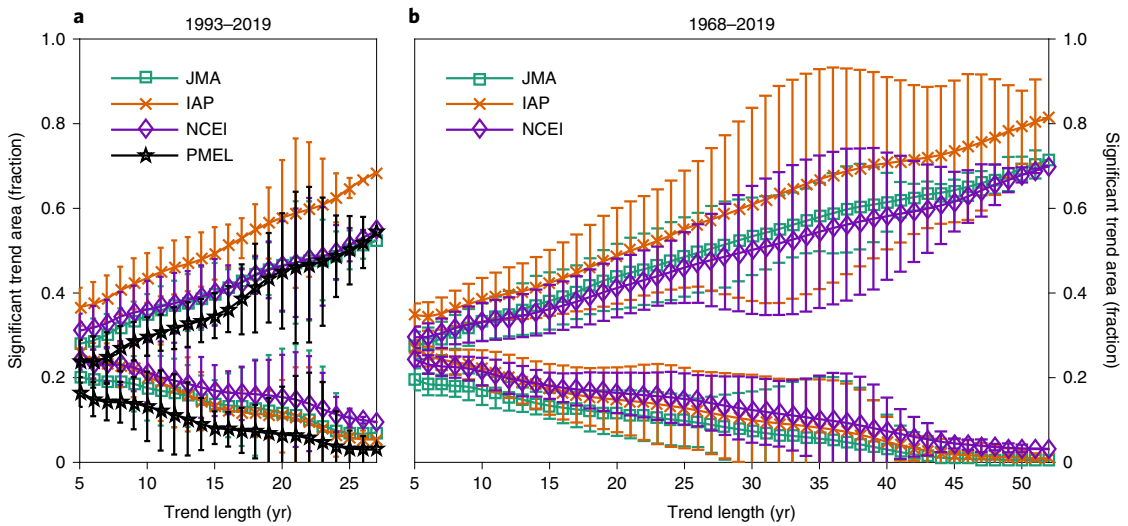

Fig. 3 | Mean fractions of the global ocean surface area with trends of upper-ocean heat content that are statistically significantly different from zero. **a**,**b**, Annual maps from four research groups are used for 1993–2019 (**a**) and 1968–2019 (**b**). Areas of statistically significant positive trends increase with increasing trend length, and areas of statistically significant negative trends decrease with increasing trend length. Mean and uncertainties are estimated using all possible contiguous periods from 5-yr (left side, 43 estimates) to 27-yr (**a**, right side, only one estimate) or 52-yr (**b**, right side, only one estimate) trend lengths. Error bars show 90% two-tailed confidence limits using the variance of the estimates and Student's *t* distribution, estimating the degrees of freedom as the record length (27 or 52 yr) divided by the trend length (5 to 27 yr or 52 yr). Since there is only one realization for the record-length trends, their uncertainties are not estimated.

longer periods are monotonic for all the maps. These positive and negative areas are generally statistically distinct with respect to estimates of their 5–95% confidence limits (see Methods for details) for ≥7-yr periods for all the different products used in the 1993–2019 analysis (Fig. 3a).

While the areas with statistically significant positive and negative 5-yr trends are quite similar for the 1993–2019 (Fig. 3a) and 1968–2019 (Fig. 3b) analyses, the latter are statistically distinct even for 5-yr trends (Fig. 3b), probably owing to a nearly doubled record length and consequent increase in degrees of freedom. In

addition, the variance of the maps before 1993 may be smaller in some data-sparse regions (for example, south of 30° S), which could be another contributing factor. For a given trend length, the areas with statistically significant positive trends are slightly larger and those with negative trends are slightly smaller for the 1993–2019 analysis than for the 1968–2019 analysis. This difference (which is well within the uncertainties) is probably owing to a stronger global warming signal in more recent times. However, it could also be owing to decreased data coverage in earlier years, which will generally tend to bias the maps for those years towards the climatological values, potentially reducing warming trends during those times.

The global integral of the local record-length trends for annual 1993–2019 upper-ocean heat content PMEL maps yields a heating rate of 212 TW, equivalent to 0.42 W m^{-2} applied to the entire surface area of Earth (5.10×10^{12} m^2) over the entire 27-yr record. This result fits well within confidence limits of trend estimates from six groups based solely on in situ observations for upper ocean from 1993 to 2018, which range from 0.36 (±0.15) to 0.42 (±0.06) W m^{-2} (Ref. [19]). This good agreement of the global estimates for the combined altimeter/in situ PMEL maps with in situ-only estimates is reassuring, since determining the precise value of a relatively small residual global average value from a field with much larger regional variations is not trivial.

Both the 1993–2019 (Fig. 1) and the 1968–2019 (Fig. 2) ocean heat content trends from all the research groups yield very consistent large-scale patterns for each period. However, the trends for the two periods have somewhat different regional patterns. These patterns are mostly linked to previously reported climate phenomena. We will focus on the better-sampled 1993–2019 trends (Fig. 1). For example, from 1993 to 2019 there is a pronounced warming associated with each of the subtropical western boundary currents: the Gulf Stream in the North Atlantic, the Brazil Current in the South Atlantic, the Agulhas Current in the South Indian, the Kuroshio in the North Pacific, the East Australia Current in the South Pacific and, to a lesser extent perhaps, even the Somali Current in the North Indian Ocean. These areas of stronger warming are consistent with that found in sea surface temperature analysis and have been linked to an intensification and poleward shift of the western boundary currents associated with changes in the surface winds[23]. However, the cooling trends equatorward of the Gulf Stream extension, Kuroshio extension and Agulhas retroflection observed here indicate reductions in the upper-ocean baroclinic shear with time in these regions. This pattern has been noted previously for the Gulf Stream extension and even linked to a possible reduction in the Atlantic Meridional Overturning Circulation (AMOC)[24]. The pattern along the Kuroshio has been studied and is more complex but also shows reductions in strength in the downstream region[25].

A pronounced upper-ocean warming trend from 1993 to 2019 in the Southern Hemisphere extends across the South Atlantic, the South Indian and much of the South Pacific oceans (Fig. 1) and stores much of the oceans' long-term GHG warming[5,6]. This pattern has been observed over both shorter[5,15] and longer[26,27] periods (including 1968–2019, see Fig. 2) and is seen in an analysis of climate model projections[28]. It may be largely owing to upwelling of very old waters in the Southern Ocean, their uptake of heat in adjustment to present surface conditions, and subsequent subduction and northward spread into the subtropical gyre[29]. However, its structure has also been linked in part to a spin-up of the subtropical gyres with changes in surface winds[5,15].

In the Pacific Ocean, statistically significant (see Methods) 1993–2019 warming trends are present in the centres of the North and South Pacific basins in the vicinities of the western boundary current extensions and the western tropics (Fig. 1). Weak trends, with small areas of cooling, are present in the eastern tropics, eastern sides of the basins and high latitudes. This pattern is reminiscent of the PDO[30] in the North Pacific and the Interdecadal Pacific Oscillation[31] in both hemispheres. Temperature anomalies in the PDO and Interdecadal Pacific Oscillation and in the North Pacific have been linked to sea level and circulation changes[13]. The PDO does trend downwards from 1993 to 2019, with a trend fit to index values dropping by 0.45 over that period. By contrast, the drop is only 0.30 for a trend fit to the PDO from 1968 to 2019, and the PDO pattern in the ocean heat content trends over that period is not as distinct (Fig. 2) as for the shorter, more recent period (Fig. 1).

In the tropical Pacific, a rapid rate of increasing sea level (associated with the upper-ocean warming) in the western portion of the basin has been associated with increases in trade winds[32], although that pattern reversed over the past few years[33]. While that western Pacific increase is visible in the 1993–2019 trends (Fig. 1), it is not in the 1968–2019 trends (Fig. 2).

The upper Indian Ocean 1993–2019 ocean heat content trends exhibit warming almost throughout for both 1993–2019 (Fig. 1) and 1968–2019 (Fig. 2), again with stronger warming in the Southern Hemisphere. A strong warming trend in sea surface temperature has been reported previously there, and attributed to both GHG warming and changes in the character of El Niño in recent decades[34]. The size of the warming trend is substantially smaller for the longer period, consistent with an increased warming rate in recent decades.

The 1993–2019 trend towards a warmer upper ocean (and higher sea levels) along the east coast of North America and cooling (with lower sea levels) in the subpolar North Atlantic (Fig. 1) is highly reminiscent of a pattern that has been linked to a reduction in the strength of the AMOC in models[35]. Similar trends are visible for the 1968–2019 period, with the subpolar cooling muted over the longer period. A reduction in AMOC strength starting in 2009 relative to 2004–2008 has also been documented observationally and discussed[36], with 2004 being the first year of AMOC observations with a trans-Atlantic moored array. Our analysis indicates that the changes are large and long-term enough to support a statistically significant pattern in the 1993–2019 trends of upper-ocean heat content and even the 1968–2019 trends. However, the link of the cooling in the subpolar North Atlantic to reductions in the AMOC is difficult to disentangle, with a strong interannual cool event centred around 2015 being caused mostly by strong heat loss from the ocean to the atmosphere, rather than reduced advection of warm water northward associated with an AMOC reduction, which is expected to occur on longer timescales[37].

While the regional variations of upper-ocean heat content trends are large, even for all possible 5-yr periods in the records, the average total area of the ocean with statistically significant positive trends for all possible 5-yr periods from 1993 to 2019 using the PMEL maps, 24%, is substantially larger than that with statistically negative trends, 17% (Fig. 3). For the 27-yr 1993–2019 trend, this difference increases to 53% of the ocean area with statistically significant positive trends versus 3% of the ocean area with statistically significant negative trends. The PMEL, JMA, IAP and NCEI maps show similar patterns for 1993–2019 (Fig. 1) and the latter three for 1968–2019 (Fig. 2), with similar statistics for the record-length trends (Fig. 3 and Table 1). The means, standard deviations and ratios of their magnitudes computed for the record-length trends from maps of all the research groups show large areas of agreement (Extended Data Fig. 1). The asymmetry for the 1968–2019 record-length trends is even more pronounced than for the 1993–2019 trends (Fig. 3 and Table 1). For the 52-yr 1968–2019 trends, from 72% to 79% of the ocean area has statistically significant positive trends versus the 1% to 3% of the ocean area with statistically significant negative trends. It may take a long time for the long-term global warming signals in upper-ocean heat content or sea level[17] to emerge in the face of interannual to multidecadal variability. Even so, comparisons of observed ocean heat content trends, observed sea-level trends and those from climate models provide valuable insights[38,39]. Moreover,

not only does the global average show a clear trend, but for ≥7-yr trends, distinctly (in a statistically significant sense) more of the ocean area shows statistically significant positive trends than shows statistically significant negative trends.

Online content

Any methods, additional references, Nature Research reporting summaries, source data, extended data, supplementary information, acknowledgements, peer review information; details of author contributions and competing interests; and statements of data and code availability are available at https://doi.org/10.1038/s41558-020-0822-0.

Received: 14 August 2019; Accepted: 22 May 2020;
Published online: 13 July 2020

References

1. IPCC *Climate Change 2013: The Physical Science Basis* (eds Stocker, T. F. et al.) (Cambridge Univ. Press, 2013).
2. Cazenave, A. et al. Global sea-level budget 1993–present. *Earth Syst. Sci. Data* **10**, 1551–1590 (2018).
3. Meyssignac, B. et al. Measuring global ocean heat content to estimate the Earth energy imbalance. *Front. Mar. Sci.* **6**, 432 (2019).
4. Johnson, G. C., Lyman, J. M. & Loeb, N. G. Improving estimates of Earth's energy imbalance. *Nat. Clim. Change* **6**, 639–640 (2016).
5. Roemmich, D. et al. Unabated planetary warming and its ocean structure since 2006. *Nat. Clim. Change* **5**, 240–245 (2015).
6. Wijffels, S., Roemmich, D., Monselesan, D., Church, J. & Gilson, J. Ocean temperatures chronicle the ongoing warming of Earth. *Nat. Clim. Change* **6**, 116–118 (2016).
7. Abraham, J. P. et al. A review of global ocean temperature observations: implications for ocean heat content estimates and climate change. *Rev. Geophys.* **51**, 450–483 (2013).
8. Lyman, J. M. & Johnson, G. C. Estimating global ocean heat content changes in the upper 1800 m since 1950 and the influence of climatology choice. *J. Clim.* **27**, 1945–1957 (2014).
9. Roemmich, D. et al. On the future of Argo: a global, full-depth, multi-disciplinary array. *Front. Mar. Sci.* **6**, 439 (2019).
10. Johnson, G. C. & Birnbaum, A. N. As El Niño builds, Pacific Warm Pool expands, ocean gains more heat. *Geophys. Res. Lett.* **44**, 438–445 (2017).
11. Roemmich, D. & Gilson, J. The global ocean imprint of ENSO. *Geophys. Res. Lett.* **38**, L13606 (2011).
12. Palanisamy, H., Meyssignac, B., Cazenave, A. & Delcroix, T. Is anthropogenic sea level fingerprint already detectable in the Pacific Ocean? *Environ. Res. Lett.* **10**, 084024 (2015).
13. Wills, R. C. J. et al. Ocean circulation signatures of North Pacific decadal variability. *Geophys. Res. Lett.* **46**, 1690–1701 (2019).
14. Kenigson, J. S., Han, W. Q., Rajagopalan, B., Yanto & Jasinsk, M. Decadal shift of NAO-linked interannual sea level variability along the US northeast coast. *J. Clim.* **31**, 4981–4989 (2018).
15. Roemmich, D., Gilson, J., Sutton, P. & Zilberman, N. Multidecadal change of the South Pacific Gyre circulation. *J. Phys. Oceanogr.* **46**, 1871–1883 (2016).
16. Carson, M. & Harrison, D. E. Regional interdecadal variability in bias-corrected ocean temperature data. *J. Clim.* **23**, 2847–2855 (2010).
17. Richter, K. & Marzeion, B. Earliest local emergence of forced dynamic and steric sea-level trends in climate models. *Environ. Res. Lett.* **9**, 114009 (2014).
18. Blunden, J. & Arndt, D. S. State of the climate in 2018. *Bull. Am. Meteorol. Soc.* **100**, Si–S305 (2019).
19. Johnson, G. C. et al. in *State of the Climate in 2019* (Ed. Lumpkin, R.) S74–S77 (American Meteorological Society, 2019).
20. Ishii, M. et al. Accuracy of global upper ocean heat content estimation expected from present observational data sets. *Sola* **13**, 163–167 (2017).
21. Cheng, L. J. et al. Improved estimates of ocean heat content from 1960 to 2015. *Sci. Adv.* **3**, e1601545 (2017).
22. Levitus, S. et al. World ocean heat content and thermosteric sea level change (0-2000 m), 1955-2010. *Geophys. Res. Lett.* **39**, L10603 (2012).
23. Wu, L. X. et al. Enhanced warming over the global subtropical western boundary currents. *Nat. Clim. Change* **2**, 161–166 (2012).
24. McCarthy, G. D., Joyce, T. M. & Josey, S. A. Gulf Stream variability in the context of quasi-decadal and multidecadal Atlantic climate variability. *Geophys. Res. Lett.* **45**, 11257–11264 (2018).
25. Wang, Y. L. & Wu, C. R. Discordant multi-decadal trend in the intensity of the Kuroshio along its path during 1993-2013. *Sci. Rep.* **8**, 14633 (2018).
26. Chen, X. Y. & Tung, K. K. Varying planetary heat sink led to global-warming slowdown and acceleration. *Science* **345**, 897–903 (2014).
27. Liu, W., Xie, S. P. & Lu, J. Tracking ocean heat uptake during the surface warming hiatus. *Nat. Commun.* **7**, 10926 (2016).
28. He, C. F., Liu, Z. Y. & Hu, A. X. The transient response of atmospheric and oceanic heat transports to anthropogenic warming. *Nat. Clim. Change* **9**, 222–226 (2019).
29. Armour, K. C., Marshall, J., Scott, J. R., Donohoe, A. & Newsom, E. R. Southern Ocean warming delayed by circumpolar upwelling and equatorward transport. *Nat. Geosci.* **9**, 549 (2016).
30. Mantua, N. J., Hare, S. R., Zhang, Y., Wallace, J. M. & Francis, R. C. A Pacific interdecadal climate oscillation with impacts on salmon production. *Bull. Am. Meteorol. Soc.* **78**, 1069–1079 (1997).
31. Salinger, M. J., Renwick, J. A. & Mullan, A. B. Interdecadal Pacific Oscillation and South Pacific climate. *Int. J. Climatol.* **21**, 1705–1721 (2001).
32. Merrifield, M. A. & Maltrud, M. E. Regional sea level trends due to a Pacific trade wind intensification. *Geophys. Res. Lett.* **38**, L21605 (2011).
33. Hamlington, B. D. et al. An ongoing shift in Pacific Ocean sea level. *J. Geophys. Res. Oceans* **121**, 5084–5097 (2016).
34. Roxy, M. K., Ritika, K., Terray, P. & Masson, S. The curious case of Indian Ocean warming. *J. Clim.* **27**, 8501–8509 (2014).
35. Caesar, L., Rahmstorf, S., Robinson, A., Feulner, G. & Saba, V. Observed fingerprint of a weakening Atlantic Ocean overturning circulation. *Nature* **556**, 191 (2018).
36. Smeed, D. A. et al. The North Atlantic Ocean Is in a state of reduced overturning. *Geophys. Res. Lett.* **45**, 1527–1533 (2018).
37. Josey, S. A. et al. The recent Atlantic cold anomaly: causes, consequences, and related phenomena. *Annu. Rev. Mar. Sci.* **10**, 475–501 (2018).
38. Durack, P. J. et al. Quantifying underestimates of long-term upper-ocean warming. *Nat. Clim. Change* **4**, 999–1005 (2014).
39. Durack, P. J. et al. Ocean warming: from the surface to the deep in observations and models. *Oceanography* **31**, 41–51 (2018).

Methods

We combine altimeter and in situ ocean temperature data to produce annual maps of upper-ocean heat content anomalies following ref. [18], referring to them as the PMEL maps throughout. This well-validated method uses regional-scale correlations between ocean heat content and sea-surface height anomalies to generate a first-guess map of ocean heat content directly from sea-surface height. (Where values are missing from the altimeter maps, the first-guess map is set to zero.) It then estimates an innovation by objectively mapping the residuals of in situ ocean heat content values relative to the first-guess map, finally adding that innovation map to the first-guess map. We also use annual maps of upper-ocean heat content anomalies produced from in situ temperature data alone from three other research groups: JMA[20], IAP[21] and NCEI[22].

The Ssalto/Duacs (Segment sol multi-missions d'altimitrie, d'orbitographie et de localisation précise/data unification and altimeter combination system) global maps of satellite-altimeter-derived sea-surface height anomalies used for the PMEL maps were produced and distributed by the Copernicus Marine and Environment Monitoring Service and downloaded in January 2019. The in situ Argo data used for the PMEL maps (doi:10.17882/42182#61117) were downloaded from the US Argo Global Data Assembly Center in January 2019. The historical in situ temperature data other than Argo used for the PMEL maps were EN3 v2a[40] from the UK Met Office, derived mostly from the World Ocean Database[41] with updated mechanical bathythermograph and XBT bias corrections[42] already applied. While EN3 v2a has been superseded, there is not much change in more recent versions aside from the addition of Argo data, which we download from the primary source. The JMA, IAP and NCEI maps used are all publicly available at web addresses noted in Data availability.

While the combined altimeter method used for the PMEL maps is thoughtfully designed and carefully validated[18], agreement between local estimates or the global integrals of the combined map trends and those from in situ-only maps is not assured; the in situ data prior to Argo are sparse[8] and subject to biases[7], and the altimeter sea-surface height values are not a perfect proxy for upper-ocean heat content. After all, sea level also includes a large component from addition of mass from land ice, changes in temperature below 700 m and contributions from changing salinity. The full-depth ocean thermal expansion is estimated to account for 42% of the sea-level trend over that period[2], and the upper-ocean contribution is only a portion of that, albeit a large portion.

For all four sets of maps (PMEL, JMA, NCEI and IAP), we use annual maps at half-year intervals (that is, 50% overlapping) of ocean heat content anomaly centred on the mid-year (July 2) and the turn of the year (January 1) from July 1993 (or July 1968) through July 2019. The combined method takes advantage of the near-global coverage of sea-surface height anomalies that started in 1993 to allow well-constrained global maps of upper-ocean heat content anomalies even prior to Argo first reaching sparse global coverage around 2005. Without these first guesses, before the advent of near-global Argo coverage in the mid-2000s, large data-sparse areas of the PMEL maps south of ~30° S would be relatively featureless with near-zero (climatological) values[8]. Maps are generated over the entire ocean surface area, which is 361×10^{12} m^2. For the in situ maps for other research groups, the area mapped varies slightly and is not quite global for some.

To account for the varying instrument types and take the best advantage of their typical depths of maximum measurements[7], the PMEL analysis is done in six carefully chosen depth layers (0–40 m, 40–90 m, 90–190 m, 190–290 m, 290–450 m and 450–700 m) following ref. [8]. The use of depth layers allows use of the full vertical resolution of the in situ temperature profiles. Our aim in using these specific layer depths is to maximize the number of profiles spanning each layer.

The annual PMEL maps, because they incorporate information from individual in situ profiles as well as spatially detailed maps of sea-surface height from altimeter data, resolve (or at least permit) eddy scales[19]. However, the signatures of eddies and other mesoscale variability are noise for our purposes. Hence, we suppress them by filtering each annual map with a two-dimensional Hanning filter that has half-maxima at 6° longitude and 3° latitude length scales prior to analysis. Before smoothing, we linearly interpolate spatially to fill gaps in the maps, allowing the subsequent smoothed fields to extend to ocean boundaries, hence not reducing the analysed areas at the edges of mapped regions by smoothing. While the results are relatively insensitive to the application of the smoothing step, or variations in the smoothing length scales, the spatial patterns revealed in our analyses are slightly clearer visually and slightly more robust statistically when using the smoothed fields instead of the unsmoothed fields. The results from the smoothed maps are also more similar to the in situ maps made by other research groups, which generally employ larger mapping scales than the PMEL maps because in situ data do not usually resolve eddy scales. Hence, we proceed with the smoothed PMEL maps.

After smoothing, we mask each depth layer using ETOPO2 (2′ Earth Topography) bathymetry[43] smoothed with a 0.5° latitude × 0.5° longitude half-width Hanning filter. We weight the mask using the fraction of the layer present when the smoothed bottom depth at a gridpoint is shallower than the bottom of a layer but deeper than the top of that layer. We then add the masked maps for all layers to make a single 0–700 m layer for analysis.

After smoothing, masking and summing the layers, we then fit local linear regressions to the resulting fields at each location over periods ranging from 5 to 27 yr (for 1993–2019) for the combined maps. We perform an identical analysis to the in situ-only based maps from the other research groups, and add analysis for 5 to 52 yr (for 1968–2019) for those maps, which extend back further in time than 1993.

All analyses use the residuals of the simple least-squares linear fits to find standard errors of the slopes in the regular fashion[44]. We also take into account the effective degrees of freedom for serial correlation in those residuals by using twice the integral of the lagged autocorrelation as an estimate of the decorrelation timescale[45]. We express all estimate uncertainties as 90% two-tailed (5–95%) confidence intervals, assuming Student's t distribution. While many different choices of confidence intervals could be made, 90% two-tailed (5–95%) confidence intervals are also used in the Fifth Assessment Report of Working Group One to the IPCC[1] and for ocean heat content analyses in annual State of the Climate reports[19]. The uncertainties increase with trend length as the degrees of freedom decrease until reaching about two-thirds to the quarters of the record length (Fig. 3). For the longer trend lengths, the uncertainties decrease, probably because even the application of Student's t distribution does not quite make up for the lack of independence in those records.

Data availability

The Ssalto/Duacs global maps of satellite-altimeter-derived sea-surface height anomalies used for the PMEL maps were downloaded in January 2019 and can be accessed at https://www.aviso.altimetry.fr/en/data/products/sea-surface-height-products/global.html. The in situ Argo data used for the PMEL maps (https://doi.org/10.17882/42182#61117) were downloaded from the US Argo Global Data Assembly Center in January 2019 and can be accessed at https://www.usgodae.org//argo/argo.html. The historical in situ temperature data other than Argo used for the PMEL maps were EN3 v2a from www.metoffice.gov.uk/hadobs. This version has been superseded, but historical non-Argo data in later versions are very similar. The ocean heat content maps from JMA can be accessed at https://www.data.jma.go.jp/gmd/kaiyou/english/ohc/ohc_global_en.html, those from IAP at http://159.226.119.60/cheng/ and those from NCEI at https://www.nodc.noaa.gov/OC5/3M_HEAT_CONTENT/.

References

40. Ingleby, B. & Huddleston, M. Quality control of ocean temperature and salinity profiles—historical and real-time data. *J. Mar. Syst.* **65**, 158–175 (2007).
41. Locarnini, R. A. et al. *World Ocean Atlas 2009, Volume 1: Temperature* (US Government Printing Office, 2010).
42. Ishii, M. & Kimoto, M. Reevaluation of historical ocean heat content variations with time-varying XBT and MBT depth bias corrections. *J. Oceanogr.* **65**, 287–299 (2009).
43. Smith, W. H. F. & Sandwell, D. T. Global sea floor topography from satellite altimetry and ship depth soundings. *Science* **277**, 1956–1962 (1997).
44. Wunsch, C. *The Ocean Circulation Inverse Problem* (Cambridge Univ. Press, 1996).
45. von Storch, H. & Zwiers, F. W. *Statistical Analysis in Climate Research* (Cambridge Univ. Press, 1999).

Acknowledgements

G.C.J. and J.M.L. are supported by the Global Ocean Monitoring and Observing programme, National Oceanic and Atmospheric Administration (NOAA), US Department of Commerce and NOAA Research. The Argo data used here were collected and made freely available by the International Argo Program and the national programmes that contribute to it (http://www.argo.ucsd.edu, http://argo.jcommops.org). The Argo Program is part of the Global Ocean Observing System. The Ssalto/Duacs altimeter products were produced and distributed by the Copernicus Marine and Environment Monitoring Service (CMEMS) (http://www.marine.copernicus.eu). We thank chief editor B. Wake for helpful comments and suggestions. The scientific results and conclusions, as well as any views or opinions expressed herein, are those of the authors and do not necessarily reflect the views of NOAA or the Department of Commerce. PMEL Contribution number 4968.

Author contributions

G.C.J and J.M.L designed the study. J.M.L. made the calculations and analysed the trends. G.C.J. wrote the manuscript. Both authors contributed to interpreting the results and improving the manuscript.

Competing interests

The authors declare no competing interests.

Additional information

Extended data is available for this paper at https://doi.org/10.1038/s41558-020-0822-0.

Correspondence and requests for materials should be addressed to G.C.J.

Peer review information *Nature Climate Change* thanks Karina von Schuckmann and the other, anonymous, reviewer(s) for their contribution to the peer review of this work.

Reprints and permissions information is available at www.nature.com/reprints.

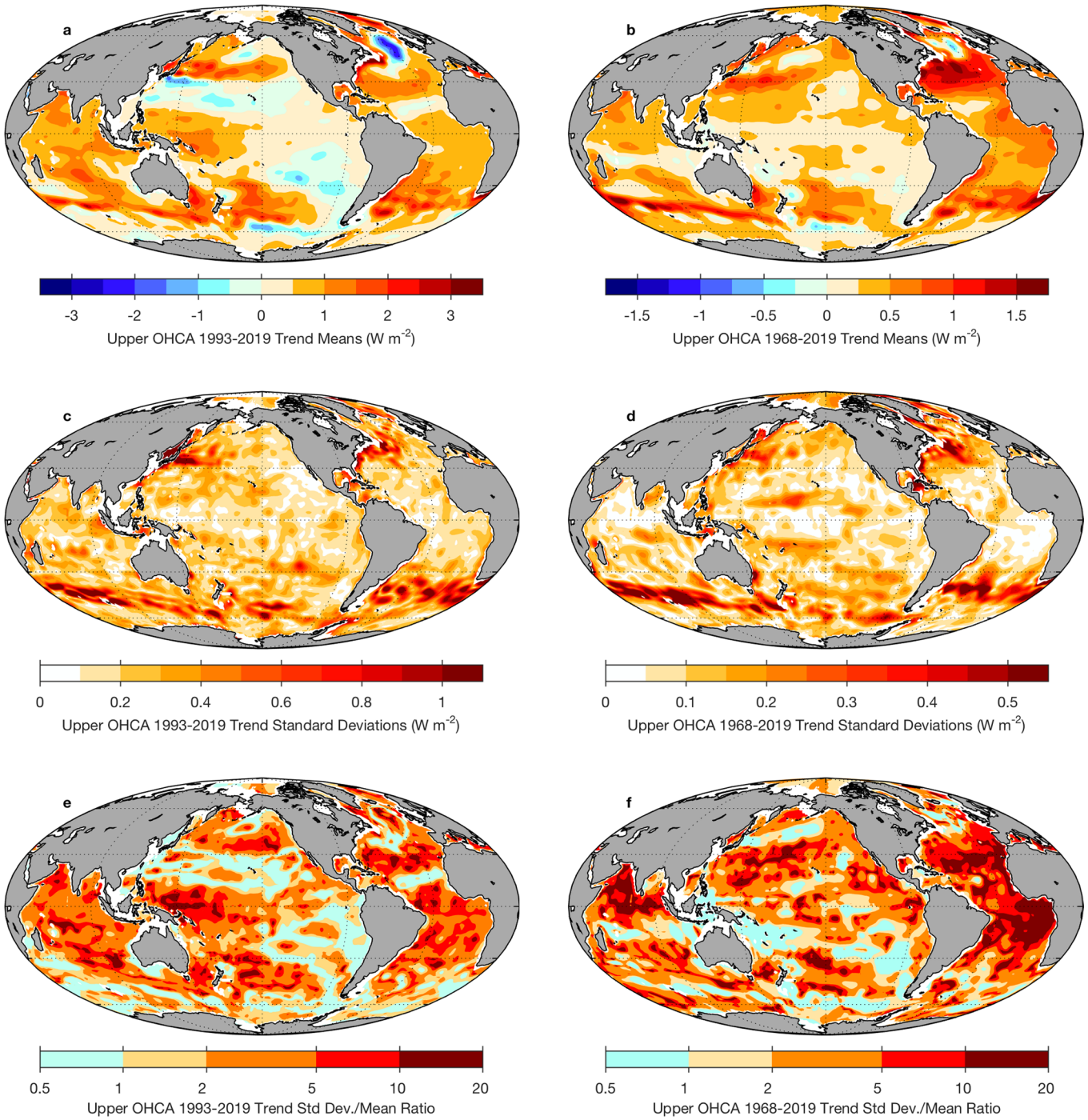

Extended Data Fig. 1 | Maps of means, standard deviations, and ratios of their magnitudes for the different 0–700 m ocean heat content trend estimates used. Means of trends for (**a**) 1993–2019 are contoured over twice the range used for (**b**) 1968–2019. Similarly, the standard deviations for (**c**) 1993–2019 trends are contoured over twice the range used for (**d**) 1968–2019. The ratio of the mean trend magnitudes to their standard deviations are contoured on the same scale for (**e**) 1993–2019 and (**f**) 1968–2019. Latitudes are gridded at 30° intervals, and longitudes, centered on 150 °W, at 60° intervals (dotted lines).